Statistical stability of correlation based imaging algorithms

M. Leibovich[*], G. Papanicolaou[†] and C Tsogka[‡]

March 20, 2024

Abstract

We consider imaging of an airborne target and study the stability of correlation based imaging methods to random fluctuations in the target's motion. The imaging system consists of a ground based emitter, and several passive receivers. By migrating the cross correlations of the received signals the two-point interference matrix is obtained. An image is then formed either by taking the diagonal of this matrix or by computing the eigenvector corresponding to the largest eigenvalue of the matrix. We call the latter the rank-1 imaging method. We show that the rank-1 image exhibits exceptional stability with respect to fluctuations in the platform's motion. We relate that to the stability of the first eigenvector of a matrix perturbed by multiplicative random phase noise. We provide simulations as well as an analytical model that demonstrates the robustness of the rank-1 imaging method to random fluctuations in the target's motion.

1 Introduction

Accurate radar imaging of moving airborne targets by ground based receivers is of great importance in many defence and civilian applications. Energy and operational signal to noise ratio constraints favor the use of inverse synthetic aperture radar (iSAR) systems, where the target is probed by a train of consecutive pulses sent from a source located at $\mathbf{x_E}$ and the echoes are recorded at receivers with positions $\mathbf{x_R}$, as illustrated in Figure 1. The received echoes are then processed coherently to form an image [6, 5, 13]. A commonly used method is migration, where the echoes are translated by the travel time to a candidate target location, coherently interfering when there is indeed a scatterer at that location.

A major challenge for SAR systems is the motion of the target in between different probing pulses. The motion needs to be compensated in order to achieve a high resolution image [9]. In this paper, we consider the robustness of different migration imaging schemes to random fluctuations in the target trajectory.

[1]Courant Institute of Mathematical Sciences, New York University, New York, NY
[2]Department of Mathematics, Stanford University, Stanford, CA
[3]Department of Applied Mathematics, University of California, Merced, CA 95343

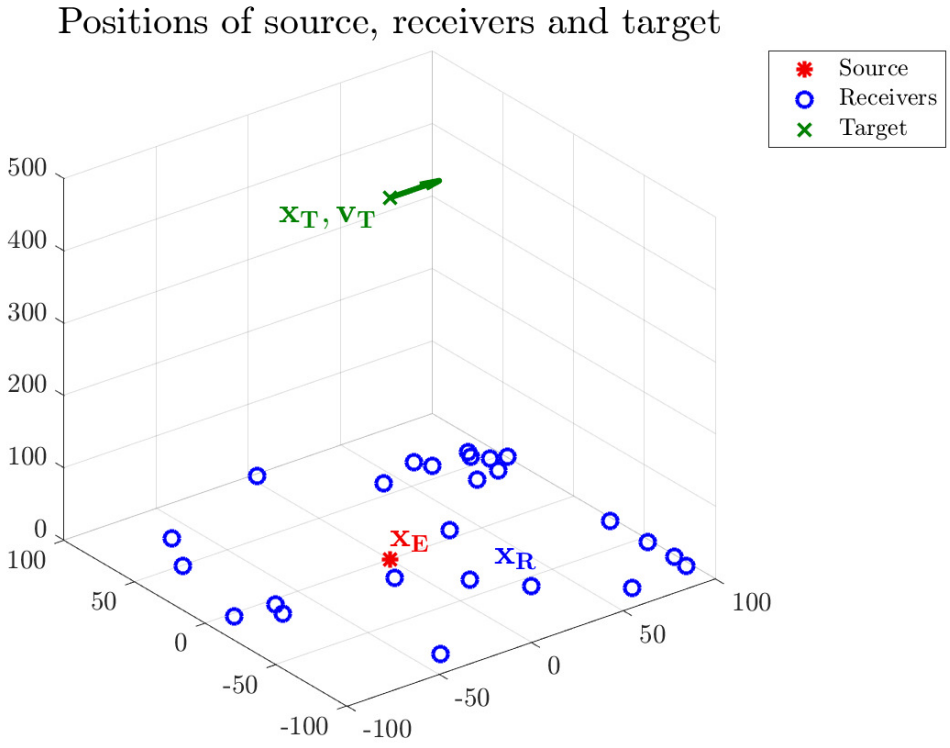

Figure 1: iSAR imaging schematic. A network of receivers with positions $\mathbf{x_R}$, is randomly distributed over a certain area. The source $\mathbf{x_E}$ is on the ground, and the target $\mathbf{x_T}$ is moving at an altitude.

1.1 Correlation based imaging methods

Correlation based imaging has been motivated by its robustness to random medium fluctuations as well as because it enables the use of asynchronous sources for probing [1, 8]. In previous work [10], we have shown that from the cross correlation measurements a natural cross-correlation data structure emerges, that in turn can be migrated to a two-point interference function. The interference function, *i.e.*, a matrix when evaluated on the imaging region of interest, can be used to form an image in one of several different ways. The diagonal of this matrix is the imaging method analyzed in [1, 8], we call this the single point migration while the top eigenvector of this matrix is the rank-1 method proposed and analyzed in [10]. Specifically, we showed that the rank-1 method achieved high resolution while maintaining the favorable properties of cross correlation imaging. Recently, the two-point interference function was also considered for imaging in random media using coherent interferometry (CINT) [3]. Several other extensions alongside the top eigenvector where examined, including an optimization method based on a Wigner-like transform of the two point interference function.

1.2 Motion compensation and SAR autofocus methods

Migration imaging is based on a travel time estimate from the source to a search point in the image domain and then from this point to the receivers. This estimate in general includes both the targets' positions and velocities. One possibility is therefore to construct an image that estimates position and velocity at the same time [2]. The main disadvantage of such an approach is that the dimension of the image domain is doubled and with it the associated computational cost of generating an image is squared. Prior information can mitigate some of the computational burden, and reduce the size of the image window in the velocity space [4].

Another set of algorithms that have been used for treating target motion is autofocus [7]. These algorithms exploit the fact that target motion introduces phase errors in the data, which can be estimated and corrected by spatio-temporal adaptive processing.

More recently, autofocus has been applied to sparsity driven imaging methods both using conventional methods [4] and deep learning [11, 12]. While these methods can achieve high resolution, for iSAR they still require a good initial estimate of the target's motion followed by intensive computations.

1.3 Main result

In this paper we study the statistical stability of correlation based imaging algorithms with respect to perturbations in the moving target's flight path. We show that the rank-1 method, in addition to achieving superior resolution, also proves to be robust to random fluctuations in the target's motion. This is illustrated with numerical simulations for single and multiple target scenarios. We also provide a theoretical analysis based on a simplified model that explains the rank-1 method's enhanced stability. Note that as the strength of the fluctuations increases, all imaging methods eventually become unstable. However, the rank-1 method remains stable for a larger range of the fluctuations strength compared to the single point migration, while traditional migration imaging (*i.e., not correlation based*) loses its coherence immediately.

The rest of the paper is as follows. In Section 2 we briefly review the SAR data model, the cross correlation data structure, and the migration imaging methods used. In Section 3.1, we present simulations that demonstrate the robustness of the rank-1 method with respect to random platform fluctuations. In Section 3.2, we present an analytical model that explains the observed robustness. We conclude with a summary and conclusions in Section 4.

2 iSAR data model and imaging methods

In this section we describe the iSAR data model used, and the different imaging methods considered.

2.1 Statement of the problem

We are interested in an inverse synthetic aperture radar (iSAR) setup, where an array of ground based receivers is used to image a moving target with velocity $\mathbf{v_T}$, as illustrated in Figure 1. The object of interest is moving and its position at time s is

$$\mathbf{x_T}(s) = \mathbf{x_T} + \mathbf{v_T} s. \tag{1}$$

The data is the collection of signals recorded at $N_\mathbf{R}$ ground based receivers, with positions $\mathbf{x_R}$. Successive pulses are emitted at a slow time s by a source located at $\mathbf{x_E}$ on the ground. The source emits a series of limited support pulses $f(t) = \cos(\omega_o t) e^{-B^2 t^2/2} \chi_{\{-3/B \le t \le 3/B\}}$, at slow time intervals of Δs, with a total aperture size S, such that the recorded signal at the receiver location $\mathbf{x_R}$ due to a pulse, $f(s+t)$, emitted at slow time $s \in [-S/2, S/2]$, is, in the single scattering (Born) approximation,

$$u_\mathbf{R}(s,t) = -\rho \frac{f''(s + t - t_\mathbf{R}(\mathbf{x_T}(s), \mathbf{x_E}, \mathbf{v_T}))}{(4\pi |\mathbf{x_T}(s) - \mathbf{x_R}|)^2}. \tag{2}$$

The derivation of (2) was carried in [10]. $t_\mathbf{R}(\mathbf{x_T}(s), \mathbf{x_E}, \mathbf{v_T})$ is the total travel time from the emitter to the target at location $\mathbf{x_T}(s)$ and from the target to the receiver $\mathbf{R}$. In [10], a Doppler factor $\gamma_\mathbf{R}$ was considered, which becomes significant for targets in Keplerian orbit, where $|\mathbf{v_T}|/c_0$ is not insignificant, with c_0 the speed of light. For simplicity, we assume for the rest of this paper that $\gamma_\mathbf{R} = 1$, and no Doppler correction is needed. As was shown in [10], the use of finite sized imaging windows allows one to take a fixed $\gamma_\mathbf{R}$, and define similar data structures to the ones used in this work.

2.2 The cross-correlation data structure in iSAR

Imaging with direct receiver data requires knowing many parameters to a high degree of accuracy to achieve a synchronous synthesis of all receiver data, including the receiver position and its waveform [8, 10]. The data is also sensitive to any medium fluctuations that affect the travel time between the source and the target and/or the target and the receivers. For that purpose, a cross correlation data structure is introduced.

We cross-correlate the measurements $u_\mathbf{R}(s,t)$ to construct $C_{\mathbf{R}\mathbf{R}'}(s,\tau)$, a cross correlation data structure, for any receiver pair $\mathbf{R}, \mathbf{R}'$ dependent on the slow time s and τ, the offset

between receiver data,

$$C_{\mathbf{R}\mathbf{R}'}(s,\tau) = \int u_{\mathbf{R}}(s, t + t_{\mathbf{R}}(\mathbf{x}_0 + s\mathbf{v}_0, \mathbf{x}_\mathbf{E}, \mathbf{v}_0)) \times \\ u_{\mathbf{R}'}(s, t + t_{\mathbf{R}'}(\mathbf{x}_0 + s\mathbf{v}_0, \mathbf{x}_\mathbf{E}, \mathbf{v}_0) + \tau) dt. \tag{3}$$

Here $t_{\mathbf{R}}(\mathbf{x}_0 + s\mathbf{v}_0, \mathbf{x}_\mathbf{E}, \mathbf{v}_0)$ is the total travel time from the source at $\mathbf{x}_\mathbf{E}$ to the center of the image window, $\mathbf{x}_0$ moving at a speed $\mathbf{v}_0$ and then from $\mathbf{x}_0$ to receiver $\mathbf{R}$. Translating both terms by $t_{\mathbf{R}}, t_{\mathbf{R}'}$, respectively, is a process known as range compression. It generates a compact data structure with limited support around $\tau = 0$ that is easier to store. We will assume that $\mathbf{v}_0 = \mathbf{v}_\mathbf{T}$ and seek to recover only the position of the target. Both $C_{\mathbf{R}\mathbf{R}'}(s,\tau)$ and $u_{\mathbf{R}}(s,t)$ can be used in migration schemes to image.

2.3 Imaging with migrated data

We summarize here the main migration methods used. For a detailed presentation see [10].

Assume we have discretized the image window relative to its moving center $\mathbf{x}_\mathbf{T}(s)$, with grid points $\mathbf{y}_k$, $k = 1, \ldots, K$. The center of the window corresponds to the point $\mathbf{0}$. The unknown reflectivity is discretized by its values on this grid

$$\rho_k = \rho(\mathbf{y}_k),\ k = 1, \ldots, K.$$

The unknown reflectivity vector has dimension K, which is the number of pixels in the image window. Imaging is the estimation of the location of the reflectors and their strength.

The signal recorded at receiver location $\mathbf{x}_\mathbf{R}$ can be written as

$$\tilde{u}_{\mathbf{R}}(s,t) \approx -\sum_{k=1}^{K} \rho_k \frac{f''(s + t - (t^k_{\mathbf{R}}(s) - t_{\mathbf{R}}(s)))}{(4\pi|\mathbf{x}_\mathbf{T}(s) - \mathbf{x}_\mathbf{R}|)^2}, \tag{4}$$

where

$$\begin{aligned} t^k_{\mathbf{R}}(s) &= t_{\mathbf{R}}(\mathbf{x}_\mathbf{T}(s) + \mathbf{y}_k, \mathbf{x}_\mathbf{E}, \mathbf{v}) \\ &= \frac{|\mathbf{x}_\mathbf{T}(s) + \mathbf{y}_k - \mathbf{x}_\mathbf{E}|}{c_0} + \frac{|\mathbf{x}_\mathbf{T}(s) + \mathbf{y}_k - \mathbf{x}_\mathbf{R}|}{c_0}, \\ t_{\mathbf{R}}(s) &= t_{\mathbf{R}}(\mathbf{x}_\mathbf{T}(s), \mathbf{x}_\mathbf{E}, \mathbf{v}), \end{aligned} \tag{5}$$

$t_{\mathbf{R}}$ is the travel time to the center of the imaging window, and $t^k_{\mathbf{R}}$ is the travel time to a discretized pixel $\mathbf{y}_k$. The difference in travel time is equivalent to range compression, making the support of the travel time distance compact around 0. In the frequency domain, the recorded signal is

$$\begin{aligned} \hat{u}_{\mathbf{R}}(s,\omega) &\approx \sum_{k=1}^{K} \frac{\omega^2 \hat{f}(\omega)}{(4\pi|\mathbf{x}_\mathbf{T}(s) - \mathbf{x}_\mathbf{R}|)^2} A_{\mathbf{R},k}(s,\omega)\rho_k, \\ A_{\mathbf{R},k}(s,\omega) &\equiv e^{i\omega(t^k_{\mathbf{R}}(s) - t_{\mathbf{R}}(s))}. \end{aligned} \tag{6}$$

The phase $A_{\mathbf{R},k}(s,\omega)$ comes from the reduced travel time from the target to the receiver, relative to that of the image window center.

We assume the distance from the reflector to the different receivers doesn't vary greatly across different receivers, hence we can approximate

$$\frac{\omega^2 \hat{f}(\omega)}{(4\pi|\mathbf{x_T}(s) - \mathbf{x_R}|)^2} \approx \xi(\omega, s), \tag{7}$$

independent of $\mathbf{R}$. By neglecting the dependence of the amplitude factor on a specific receiver, the accuracy with which the amplitude of the reflector can be retrieved is compromised but not its support.

Using this notation, and the fact that correlation in time is equivalent to multiplication in frequency, we get that

$$\begin{aligned} \hat{C}_{\mathbf{RR'}}(s,\omega) &= \hat{u}_{\mathbf{R}}(s,\omega)\overline{\hat{u}_{\mathbf{R'}}(s,\omega)} \\ &\approx |\xi(\omega,s)|^2 \sum_{k,k'=1}^{K} A_{\mathbf{R},k}(s,\omega)\overline{A_{\mathbf{R'},k'}(s,\omega)}\rho_k\rho_{k'} \end{aligned} \tag{8}$$

This is our model for the cross-correlation data in the frequency domain.

Denote by $\boldsymbol{\rho}$ the unknown reflectivities in vector form

$$\boldsymbol{\rho} = [\rho_1, \ldots, \rho_K]^T \in \mathbb{R}^K.$$

Denote $\mathcal{A}(s,\omega)$, our model for the sensing matrix. It has dimensions $N_R \times K$ and entries $A_{\mathbf{R},k}(s,\omega)$ defined in (6). This matrix $\mathcal{A}(s,\omega)$ acts on the reflectivities and returns data. Denote the recorded signal data as an N_R vector $\hat{\mathbf{u}}_{\mathbf{R}}(s,\omega)$ whose entries are given by (6). The cross-correlation data is also a matrix, of dimension $N_R \times N_R$, $\hat{\mathbf{C}}(s,\omega)$ with entries $\hat{C}_{\mathbf{RR'}}(s,\omega)$ as in (8).

Combining these, we have in matrix form the following model for the recorded signal data vector $\hat{\mathbf{u}}_{\mathbf{R}}(s,\omega)$ and cross-correlation data matrix $\hat{\mathbf{C}}(s,\omega)$

$$\hat{\mathbf{u}}_{\mathbf{R}}(s,\omega) = \xi(s,\omega)\mathcal{A}(s,\omega)\boldsymbol{\rho}, \tag{9}$$

$$\begin{aligned} \hat{\mathbf{C}}(s,\omega) &= \hat{\mathbf{u}}_{\mathbf{R}}(s,\omega)\overline{\hat{\mathbf{u}}_{\mathbf{R}}(s,\omega)}^T \\ &= |\xi(\omega,s)|^2(\mathcal{A}(s,\omega)\boldsymbol{\rho})\overline{(\mathcal{A}(s,\omega)\boldsymbol{\rho})}^T \\ &= |\xi(\omega,s)|^2\mathcal{A}(s,\omega)\boldsymbol{\rho}\boldsymbol{\rho}^T\overline{\mathcal{A}(s,\omega)}^T. \end{aligned} \tag{10}$$

Denoting by $\mathbf{X} = \boldsymbol{\rho}\boldsymbol{\rho}^T, X_{kk'} = \rho_k\rho_{k'}$, the outer product of reflectivities, then our model for the cross-correlation data in matrix form is

$$\hat{\mathbf{C}}(s,\omega) = |\xi(\omega,s)|^2\mathcal{A}(s,\omega)\mathbf{X}\overline{\mathcal{A}(s,\omega)}^T. \tag{11}$$

The cross-correlations depend on the reflectivities $\boldsymbol{\rho}$ through their outer product $\mathbf{X} = \boldsymbol{\rho}\boldsymbol{\rho}^T$. As a result, there can be several different extensions of Kirchhoff migration to cross-correlations, which we investigate in the next section. We note that up till now we assumed the measurements to be continuous functions of s, ω. In practice, both these arguments are discretized by finite sampling rates.

2.4 Imaging functions for cross-correlation data

Given the data $\hat{\mathbf{u}}_{\mathbf{R}}(s,\omega)$ and the model $\hat{\mathbf{u}}_{\mathbf{R}}(s,\omega) = \mathcal{A}(s,\omega)\boldsymbol{\rho}$, Kirchhoff migration of the data $\hat{\mathbf{u}}_{\mathbf{R}}(s,\omega)$ is given by

$$\tilde{\boldsymbol{\rho}} = \sum_{s,\omega} \overline{\mathcal{A}(s,\omega)}^T \hat{\mathbf{u}}_{\mathbf{R}}(s,\omega). \tag{12}$$

It was shown in [10] that a natural extension of (12) for migrating cross-correlations is the matrix $\tilde{\mathbf{X}}$

$$\tilde{\mathbf{X}} = \sum_{s,\omega} \overline{\mathcal{A}(s,\omega)}^T \hat{\mathbf{C}}(s,\omega)\mathcal{A}(s,\omega), \tag{13}$$

with elements

$$\tilde{X}_{kk'} = \sum_{s,\omega,\mathbf{R},\mathbf{R}'} \overline{A}_{\mathbf{R},k}(s,\omega)\hat{C}_{\mathbf{R},\mathbf{R}'}(s,\omega)A_{\mathbf{R}',k'}(s,\omega). \tag{14}$$

The result of this two-point migration is an estimation of $\mathbf{X}$ rather than $\boldsymbol{\rho}$, as our model is quadratic with respect to the reflectivities. $\tilde{\mathbf{X}}$ is a square matrix with dimensions $K \times K$, where K is the number of search points in the imaging domain. If points $\mathbf{y}_k, \mathbf{y}_{k'}$ are associated with reflectivities $\rho_k, \rho_{k'}$, we can think of $\tilde{\mathbf{X}}$ as a two-variable generalized cross-correlation imaging function

$$\mathcal{I}^{GCC}(\mathbf{y}_k, \mathbf{y}_{k'}) = \tilde{X}_{kk'}. \tag{15}$$

Note that $\tilde{\mathbf{X}} \in \mathbb{C}^{K\times K}$ is Hermitian positive definite by definition. We will refer to it as the two-point interference pattern from which the image will be obtained. We next consider how in fact an image of the reflectivity can be extracted from $\mathcal{I}^{GCC}$. The functional $\mathcal{I}^{GCC}$ defined in (15) lacks a direct physical interpretation. It evaluates the outer product of reflectivities rather than the reflectivities themselves. We examine next two ways to extract an image from $\tilde{\mathbf{X}}$:

1. Reconstruct an image of $|\rho_k|^2 = \tilde{X}_{kk}$. This is equivalent to the migration functional proposed and analyzed in [8] since the diagonal terms of $\mathcal{I}^{GCC}(\mathbf{y}_k, \mathbf{y}_{k'})$ recreate the image generated by migrating the data to the same point $\mathbf{y}_k = \mathbf{y}_{k'}$. In terms of (15) the image is evaluated by plugging in the same search point in both variables

$$\mathcal{I}^{CC}(\mathbf{y}_k) = \mathcal{I}^{GCC}(\mathbf{y}_k, \mathbf{y}_k). \tag{16}$$

2. Reconstruct an image of $|\rho_k|^2 = |\mathbf{v}_1(\tilde{\mathbf{X}})|_k^2$, i.e., calculate the top eigenvector of $\tilde{\mathbf{X}}$. In terms of (15) the image is evaluated by taking, $\mathcal{V}(\mathbf{y}_k)$, the first eigenvector of $\mathcal{I}^{GCC}(\mathbf{y}_k, \mathbf{y}_{k'})$, thought of as a matrix

$$\mathcal{I}^{R1CC}(\mathbf{y}_k) = \mathcal{V}(\mathbf{y}_k). \tag{17}$$

   We call this the **rank-1 image**.

The performance of the different imaging functions derived from the two-point interference pattern were analyzed in [8, 10], where it was shown that the rank-1 image gives rise to better resolution. In the following section we show that another favorable property of the rank-1 image is robustness to fluctuations in the target's linear motion, a critical feature in any operational system. We first show this through numerical experiments, and then provide theoretical analysis.

3 Cross correlation imaging in the presence of target's motion fluctuations

In this section, we assume the target's motion fluctuates beyond the linear motion, so that its position at time s is given by

$$\mathbf{x_T}(s) = \mathbf{x_T} + s\mathbf{v_T} + \sigma\boldsymbol{\varepsilon}(s),$$

where $\boldsymbol{\varepsilon}(s) \in \mathbb{R}^3$ is a vector-valued random Gaussian process. We assume

$$\varepsilon_i(s) \sim \mathcal{N}(0,1), \quad \mathbb{E}(\varepsilon_i(s_1)\varepsilon_j(s_2)) = \delta_{ij}\kappa(s_1 - s_2),$$

where $\kappa(s)$ is a finite-support correlation function. The fluctuations are not compensated for by the imaging function, hence as σ increases, we expect a degradation in the image quality. We first observe the behavior of the different imaging methods through numerical experiments and then follow with analysis.

3.1 Numerical experiments

We consider an iSAR system with 16 ground based receivers, randomly distributed over a region of 230m $\times$ 230m which is a realistic scenario for imaging airborne targets. The number of receivers is based on numerical experiments (not shown here) which suggest that 16 is an adequate number for randomly distributed receivers to generate a resolution comparable to the area they span in a synthetic aperture system. A target located initially at $[0\text{m}, 1500\text{m}, 1500\text{m}]$ is moving along a straight line in the x direction with a velocity of 33 m/s. The probing signal, modeled by $f(t)$, has a carrier frequency of 960MHz, and a narrow bandwidth B of 50 MHz, with a pulse repetition frequency of 100Hz. The total recording time is 15s. The receivers positions are given in Table 1. The ground based source is located at the center of the receiver domain. As discussed in [10], correlation based imaging methods can be used without knowing the exact source position and profile.

We simulate the performance of three different imaging algorithms: Kirchhoff Migration (KM) as defined in (12), diagonal (single point) correlation based migration as in (16), and rank-1 imaging as in (17). The platform motion is perturbed by random fluctuations in all directions.

The fluctuations $\boldsymbol{\varepsilon}(s)$ have variance (rms) of 1. Their correlation length is controlled by low pass filtering of their Fourier transform (see Figure 2)

$$\boldsymbol{\varepsilon}_\lambda(s) = \mathcal{F}^{-1}\left\{\mathcal{F}\{\boldsymbol{\varepsilon}(s)\}\chi_{|\omega|<\lambda}\right\}.$$

For each value of the cutoff we generate images of the moving platform using the three imaging algorithms. To measure the effect of σ, we compute the angle between the vectorized unperturbed image (obtained for $\sigma = 0$), $\mathcal{I}^0$, and the image obtained by a perturbed platform motion ($\sigma > 0$), $\mathcal{I}^\sigma$,

$$\alpha(\sigma) = \frac{\langle \mathcal{I}^\sigma, \mathcal{I}^0 \rangle}{\|\mathcal{I}^\sigma\|\|\mathcal{I}^0\|}. \tag{18}$$

The closer this angle is to one, the more robust the imaging method is.

R1	60.0413m	199.5452m	0m
R2	168.5368m	-64.8699m	0m
R3	187.9234m	-184.5065m	0m
R4	-49.0642m	-190.9474m	0m
R5	88.0487m	59.0542m	0m
R6	72.8453m	-221.0745m	0m
R7	-221.6383m	-208.1462m	0m
R8	38.6497m	-76.9780m	0m
R9	-59.8492m	66.5584m	0m
R10	188.9418m	168.5459m	0m
R11	-205.3496m	-54.3540m	0m
R12	-201.4751m	207.9233m	0m
R13	-71.7330m	-54.9372m	0m
R14	-185.6708m	93.6254m	0m
R15	-72.3121m	196.3306m	0m
R16	189.9755m	30.8248m	0m

Table 1: The receiver positions used in the simulations

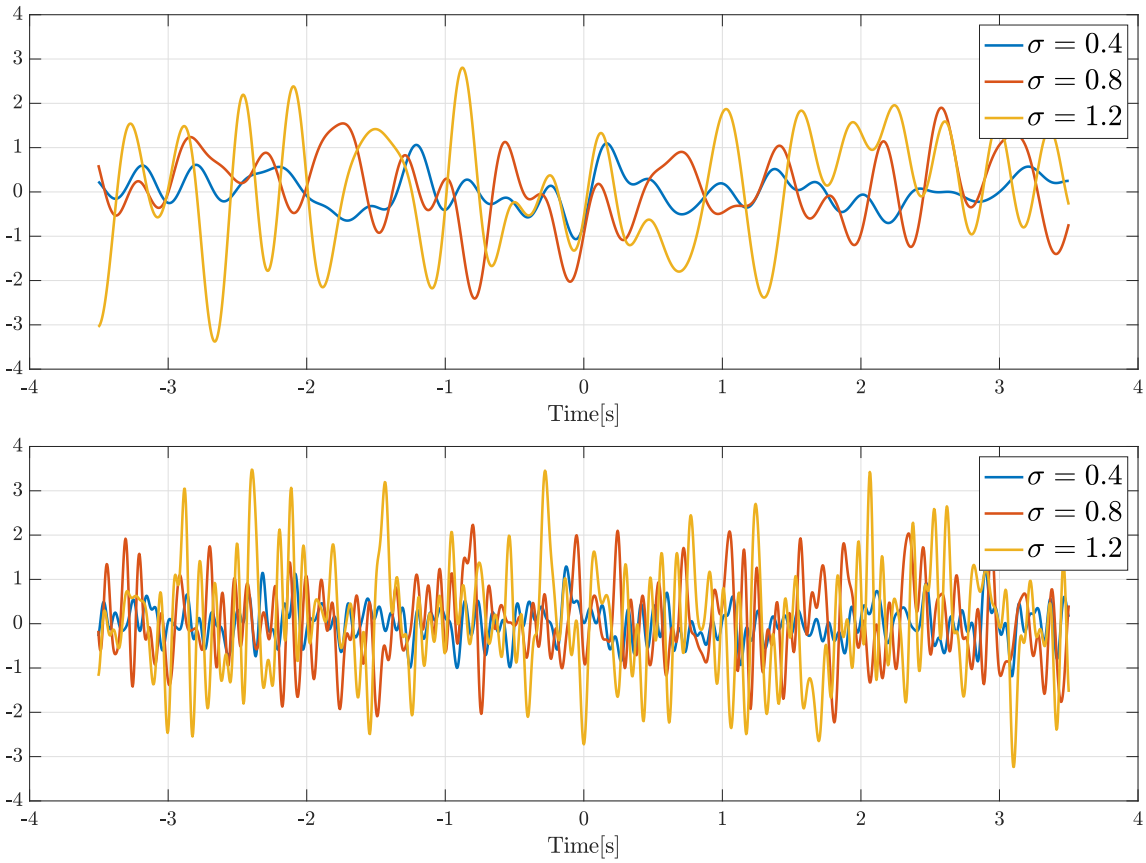

Figure 2: Platform fluctuations in meters, as a function of time for different values of the cutoff: Top 50; Bottom 200. We can see that as the cutoff increases the process becomes more oscillatory, and as a result the correlation length of the fluctuations decreases.

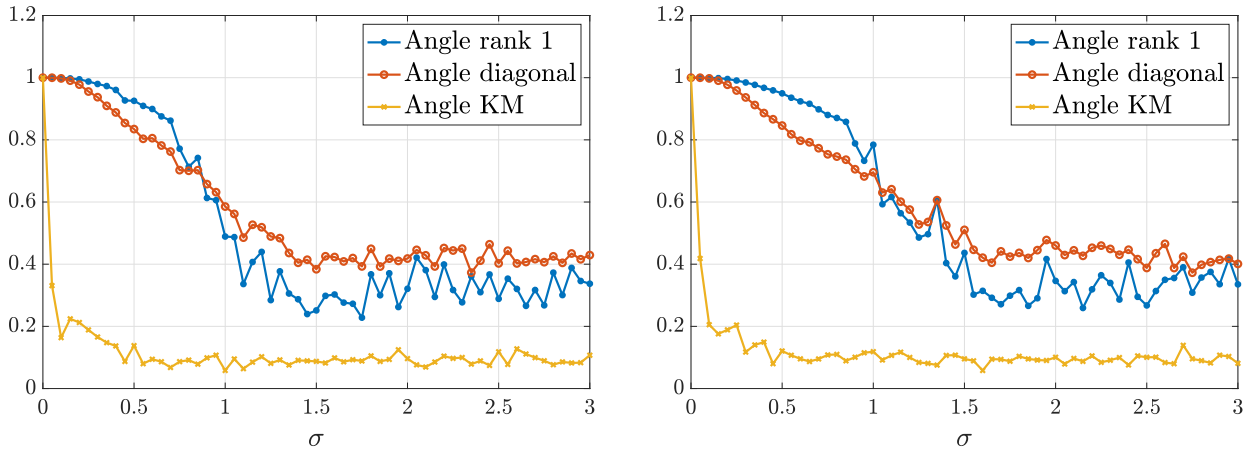

(*a*) Cutoff 50 (*b*) Cutoff 200

Figure 3: Comparison of the angle between perturbed image, $\mathcal{I}^{\sigma}$, and original image, $\mathcal{I}^{0}$. The rank-1 image, generated by the eigenvector of the two-point interference matrix, remains correlated with the unperturbed image until it exhibits a relatively sharp decay. The diagonal (single point) migration image becomes uncorrelated with the unperturbed image more gradually as σ increases. Increasing the cutoff decreases the correlation length of the platform fluctuations, resulting in an extended robustness for the rank-1 image.

As illustrated in Figure 3, Kirchhoff migration loses its correlation with the unperturbed image fairly rapidly as σ increases, signifying a deterioration in the image quality (see Figure 4-bottom row). Diagonal (single point) migration becomes uncorrelated with the unperturbed image more gradually, but still begins to lose resolution with the onset of fluctuations (see Figure 4-middle row). The rank-1 image, on the other hand, remains stable as σ increases and then a phase transition is observed as the angle decays rapidly around a value of σ which increases as the fluctuations become less correlated.

Observing the actual images generated in Figure 4-top row, we can see that indeed the rank-1 image retains its original resolution for higher values of σ than the single point migration. This motivates further investigation. In the next section we provide analysis that demonstrates that the reason for this enhanced resolution is the particular effect of the random fluctuations on the two-point interference pattern.

In Figure 5, we observe a similar behavior in a more complex setting that consists of four point scatterers. These results are encouraging and suggest that the rank-1 method has the potential of being useful for imaging more complex target geometries. More realistic scenarios including anisotropic scattering will be considered in future work.

3.2 Analysis of enhanced stability

In this section we present an analytical model to investigate the performance of the rank-1 image in the presence of motion fluctuations. We specifically show that the fluctuations affect the migrated data in a particular way, accentuating its anisotropy. As was shown in [10], The two-point interference pattern generates peaks around positions $\mathbf{y}_k, \mathbf{y}_{k'}$ that correspond to actual scatterers, with principal axes aligned with the diagonal $(\mathbf{y}_k - \mathbf{y}_{k'})$ and anti-diagonal $(\mathbf{y}_k + \mathbf{y}_{k'})$ directions. The resolution of the rank-1 image is approximately the harmonic

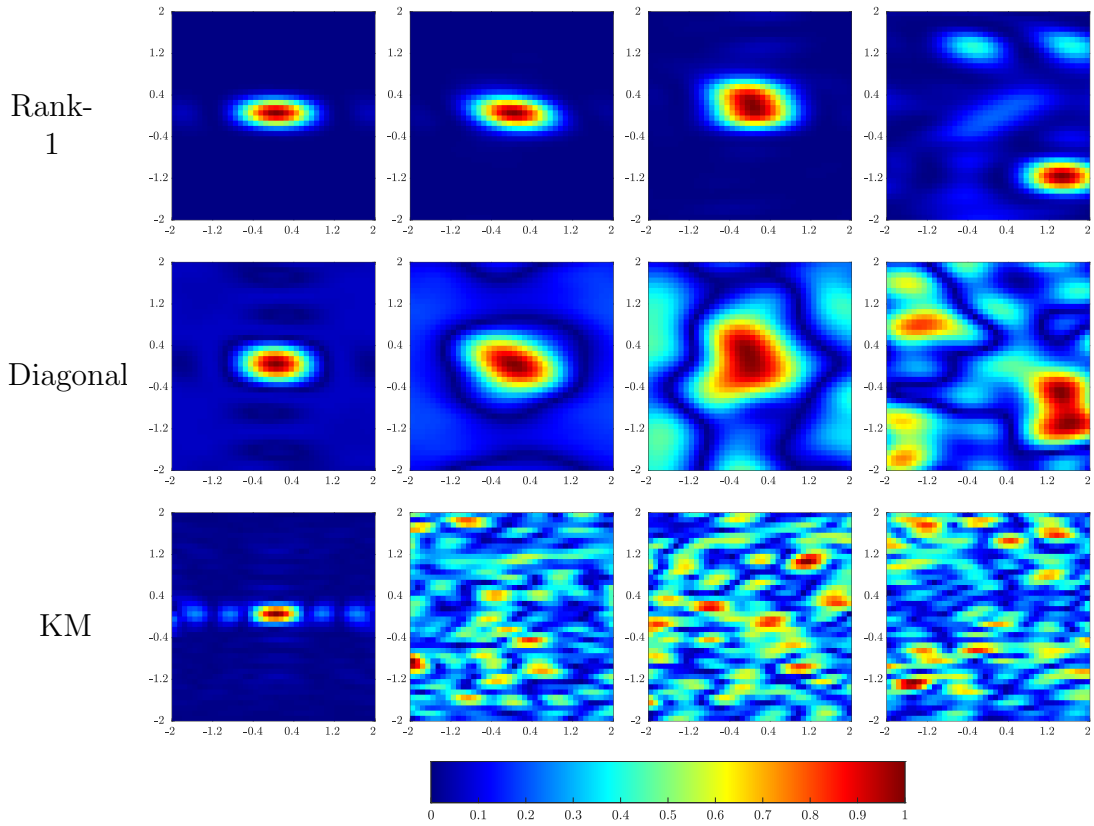

Figure 4: From top to bottom rank-1, diagonal (single point) migration and KM images for increasing rms of fluctuations. All images are normalized to take values between 0 and 1. From left to right σ increases $\sigma = 0, 0.4, 0.8, 1.2$. Note that the rank-1 image remains stable for higher values of σ, while distortion in the image appear immediately for KM. For diagonal (single point) migration the deterioration is more gradual but present event for smaller values of σ. Here cutoff equals 50, similar results (not shown here) were obtained for other cutoff values.

mean of the two principal axes of the two-point interference pattern peak. This promotes resolution as the harmonic mean is heavily biased towards the smaller, anti-diagonal axis, while the single-point migration relies on the diagonal axis, which has poorer resolution.

Denote the travel time to receiver $\mathbf{R}$ at time s from target at position $\mathbf{x} + \sigma\boldsymbol{\varepsilon}(s)$ as

$$\begin{aligned}\tau^{\mathbf{x}}_{\mathbf{R}}(s) &= \frac{1}{c}|\mathbf{x} + \sigma\boldsymbol{\varepsilon}(s) + \mathbf{x}_0(s) - \mathbf{x}_{\mathbf{R}}| \\ &\approx \frac{1}{c}|\mathbf{x}_0(s) - \mathbf{x}_{\mathbf{R}}| + \frac{1}{c}\frac{\mathbf{x}_0(s) - \mathbf{x}_{\mathbf{R}}}{|\mathbf{x}_0(s) - \mathbf{x}_{\mathbf{R}}|} \cdot (\mathbf{x} + \sigma\boldsymbol{\varepsilon}(s)) \\ &= \tau^{\mathbf{x}_0}_{\mathbf{R}}(s) + \frac{1}{c}\frac{\mathbf{x}_0(s) - \mathbf{x}_{\mathbf{R}}}{|\mathbf{x}_0(s) - \mathbf{x}_{\mathbf{R}}|} \cdot (\mathbf{x} + \sigma\boldsymbol{\varepsilon}(s))\end{aligned} \tag{19}$$

and denote,

$$\hat{d}_{\mathbf{R}}(s) = \frac{\mathbf{x}_0(s) - \mathbf{x}_{\mathbf{R}}}{|\mathbf{x}_0(s) - \mathbf{x}_{\mathbf{R}}|},$$

the direction from receiver $\mathbf{R}$ to the imaging window. The random phase that multiplies the $\mathbf{x}, \mathbf{y}$ term in the interference pattern at time s and frequency ω is

$$i\frac{\omega}{c}(\hat{d}_{\mathbf{R}}(s)-\hat{d}_{\mathbf{R}'}(s))\cdot\sigma\boldsymbol{\xi}(s). \tag{20}$$

We wish to compute $I(\mathbf{y}_k,\mathbf{y}_{k'};s,\omega)$, the two-point interference pattern generated from receiver measurements at time s and frequency ω.

$$\begin{aligned}
&I(\mathbf{y}_k,\mathbf{y}_{k'})\\
&=\sum_{s,\omega}\sum_{\mathbf{R},\mathbf{R}'}e^{-i\omega(\tau_{\mathbf{R}}^{\mathbf{y}_k}(s)-\tau_{\mathbf{R}'}^{\mathbf{y}_{k'}}(s))}\tilde{u}_{\mathbf{R}}(s,\omega)\overline{\tilde{u}_{\mathbf{R}'}(s,\omega)}\\
&\approx\sum_{s,\omega}\sum_{\mathbf{R},\mathbf{R}'}e^{-i\omega((\tau_{\mathbf{R}}^{\mathbf{y}_k}(s)-\tau_{\tilde{\mathbf{R}}}^{\mathbf{x}}(s))-(\tau_{\mathbf{R}'}^{\mathbf{y}_{k'}}(s)-\tau_{\tilde{\mathbf{R}}'}^{\mathbf{x}}(s)))}\\
&=\sum_{s,\omega}\sum_{\mathbf{R},\mathbf{R}'}e^{i\frac{\omega}{c}\hat{d}_{\mathbf{R}}(s)\cdot(\mathbf{y}_k-\mathbf{x})}e^{i\frac{\omega}{c}\hat{d}_{\mathbf{R}'}(s)\cdot(\mathbf{y}_{k'}-\mathbf{x})}\\
&\qquad\times e^{i\frac{\omega}{c}(\hat{d}_{\mathbf{R}}(s)-\hat{d}_{\mathbf{R}'}(s))\cdot\sigma\boldsymbol{\xi}(s)}
\end{aligned} \tag{21}$$

We further assume $\hat{d}_{\mathbf{R}}(s)$ can be linearized in s

$$\begin{aligned}
\hat{d}_{\mathbf{R}}&=\frac{\mathbf{x}_0-\mathbf{x}_{\mathbf{R}}}{|\mathbf{x}_0-\mathbf{x}_{\mathbf{R}}|}+\frac{\mathbf{v}_{\mathbf{T}}s}{|\mathbf{x}_0-\mathbf{x}_{\mathbf{R}}|}\\
&\approx\frac{\mathbf{x}_0-\mathbf{x}_{\mathbf{R}}}{H_{\mathbf{T}}}+\frac{\mathbf{v}_{\mathbf{T}}s}{H_{\mathbf{T}}}=d_{\mathbf{R}}+d_{\mathbf{T}}s
\end{aligned}$$

We then perform the s summation first

$$\begin{aligned}
&I(\mathbf{y}_k,\mathbf{y}_{k'})=\\
&\sum_{\omega}\sum_{\mathbf{R},\mathbf{R}'}e^{i\frac{\omega}{c}d_{\mathbf{R}}\cdot(\mathbf{y}_k-\mathbf{x})}e^{-i\frac{\omega}{c}d_{\mathbf{R}'}\cdot(\mathbf{y}_{k'}-\mathbf{x})}\times\\
&\sum_{s}e^{i\frac{\omega}{c}(d_{\mathbf{R}}-d_{\mathbf{R}'})\cdot\sigma\boldsymbol{\xi}(s)+i\frac{\omega}{c}d_{\mathbf{T}}s\cdot(\mathbf{y}_k-\mathbf{y}_{k'})}
\end{aligned} \tag{22}$$

The s summation reduces to an averaging or a weak law of large numbers computation. If we assume $\xi(s)\sim\mathcal{N}(0,\mathbb{I}_{3\times3})$, and that the sampling rate is high enough, so that the fluctuations are averaged on a time scale much smaller than the linear phase term, we can substitute the random phase term in (21) by its mean

$$\begin{aligned}
\sum_{s}e^{i\frac{\omega}{c}(d_{\mathbf{R}}-d_{\mathbf{R}'})\cdot\sigma\boldsymbol{\xi}(s)}&\propto\mathbb{E}\left[e^{i\frac{\omega}{c}(d_{\mathbf{R}}-d_{\mathbf{R}'})\cdot\sigma\boldsymbol{\xi}(s)}\right]\\
&=e^{-\frac{\omega^2\sigma^2}{2c^2}\|d_{\mathbf{R}}-d_{\mathbf{R}'}\|^2}
\end{aligned} \tag{23}$$

Our numerical simulations for the one dimensional imaging model presented in the next section are in agreement with this (see figures 6 and 7). This means we are limiting our integration region over $\mathbf{R},\mathbf{R}'$ to a smaller region around $d_{\mathbf{R}}=d_{\mathbf{R}'}$. Therefore we can further approximate the receiver summation in (21) as

$$\begin{aligned}
&\sum_{\mathbf{R},\mathbf{R}'}e^{i\frac{\omega}{c}d_{\mathbf{R}}\cdot(\mathbf{y}_k-\mathbf{x})}e^{-i\frac{\omega}{c}d_{\mathbf{R}'}\cdot(\mathbf{y}_{k'}-\mathbf{x})}e^{-\frac{\omega^2\sigma^2}{2c^2}\|d_{\mathbf{R}}-d_{\mathbf{R}'}\|^2}\times\\
&\qquad\operatorname{sinc}\left(\frac{\omega}{c}d_{\mathbf{T}}\cdot(\mathbf{y}_k-\mathbf{y}_{k'})\right).
\end{aligned} \tag{24}$$

Note that the argument in (24) can be recast as

$$\begin{aligned} & d_{\mathbf{R}} \cdot (\mathbf{y}_k - \mathbf{x}) - d_{\mathbf{R}'} \cdot (\mathbf{y}_{k'} - \mathbf{x}) \\ & = \frac{1}{2}(d_{\mathbf{R}} - d_{\mathbf{R}'}) \cdot (\mathbf{y}_k + \mathbf{y}_{k'} - 2\mathbf{x}) \\ & + \frac{1}{2}(d_{\mathbf{R}} + d_{\mathbf{R}'}) \cdot (\mathbf{y}_k - \mathbf{y}_{k'}). \end{aligned} \tag{25}$$

Define $\mu_1 = \frac{1}{2}\frac{\omega}{c}(d_{\mathbf{R}} - d_{\mathbf{R}'}), \mu_2 = \frac{1}{2}\frac{\omega}{c}(d_{\mathbf{R}} + d_{\mathbf{R}'})$. Then (24) can be recast as

$$\begin{aligned} \sum_{\mu_1,\mu_2 \in \mathcal{D}} & e^{i\mu_1 \cdot (\mathbf{y}_k + \mathbf{y}_{k'} - \mathbf{x})} e^{i\mu_2 \cdot (\mathbf{y}_k - \mathbf{y}_{k'})} e^{-2\sigma^2 \|\mu_1\|^2} \\ & \operatorname{sinc}\left(\frac{\omega}{c} d_{\mathbf{T}} \cdot (\mathbf{y}_k - \mathbf{y}_{k'})\right) \end{aligned} \tag{26}$$

The summation domain $\mathcal{D}$ is not cartesian so at least formally the sum is not separable, but it is so approximately. We see from (26) that resolution is different in the two directions $\mathbf{y}_k + \mathbf{y}_{k'}$ and $\mathbf{y}_k - \mathbf{y}_{k'}$. Resolution is better in the $\mathbf{y}_k + \mathbf{y}_{k'}$ direction which favors the rank-1 image. We remark that the diagonal $\mathcal{I}^{CC}(\mathbf{y}_k)$ image is obtained for $\mathbf{y}_k = \mathbf{y}_{k'}$ in which case the resolution is determined by the integration over μ_1 which is affected by the variance of the motion's fluctuations σ^2. The effect of the Gaussian weight is that we're decreasing the spectral integration domain along the $\mathbf{y}_k - \mathbf{y}_{k'}$ direction, making the spot large, and losing resolution.

It is shown in [10] that the resolution for the rank-1 image is approximately the harmonic mean of the resolution along the two directions $\mathbf{y}_k + \mathbf{y}_{k'}$ and $\mathbf{y}_k - \mathbf{y}_{k'}$. As the harmonic mean is always closer to the smaller of the two values, it is expected that the rank-1 image will be robust to the fluctuations and less affected by the loss in resolution in the $\mathbf{y}_k - \mathbf{y}_{k'}$ direction. This deterioration of resolution along the $\mathbf{y}_k - \mathbf{y}_{k'}$ direction is well illustrated with the one dimensional imaging model we consider next.

3.3 One dimensional imaging model

To support our analysis we considered a one dimensional imaging model, where the target is moving along a straight line, with fluctuations added in the transverse direction

$$\mathbf{x}_{\mathbf{T}}(s) = (v_{\mathbf{T}} s, 0), \quad \boldsymbol{\varepsilon}(s) = (0, \xi(s)). \tag{27}$$

As illustrated in Figure 6, looking at the angle between the unperturbed 1D image and the image in the presence of fluctuations we see that the results remain qualitatively the same when the complex phase is substituted for its mean.

In Figure 7, we see that the analysis of the two-point interference function agrees with the simulations. As explained earlier, the fluctuations extend the anisotropic nature of the two-point interference pattern, which favors the rank-1 image.

We further looked at the performance of the 1D model when the noise fluctuations are correlated (matching a particular cutoff value). As illustrated in Figure 8, the qualitative behavior extends even to fluctuations with a finite correlation length, justifying our analysis.

4 Summary & Conclusions

We have considered the problem of imaging moving objects using inverse synthetic aperture radar (iSAR), when the object motion fluctuates around a linear trajectory. We considered an array of ground based receivers, where either the data recorded at each receiver or their cross correlations are used for imaging. In Section 2, we reviewed the data model and different methods that can be used for imaging, namely the Kirchoff migration (KM) that uses direct measurements to image, and two correlation based methods: the diagonal (single point), introduced in [8], and the rank-1, introduced in [10].

In Section 3 we introduced a model for the object's fluctuations. We showed through simulations that the rank-1 image enjoys an enhanced stability region, as a function of the strength of the fluctuations σ. The rank-1 image remains localized and is not affected by the target fluctuations, in contrast with the other methods, which exhibit a greater degree of sensitivity. We further provided an analytical model that explains the observed behavior. We also provided a one dimensional simulation that demonstrates the validity of the model.

The results presented in this paper demonstrate the favorable properties of correlation based imaging, that go beyond the original rationale for using them. Important applications to be studied further include the introduction of more sources of uncertainty in the model such as medium fluctuations and uncertainty in receiver positions, as well as further possible extensions of the correlation based imaging function.

5 Acknowledgements

CT acknowledges support by the Air Force Office of Scientific Research (FA9550- 21-1-0196)

References

[1] L. Borcea, J. Garnier, G. Papanicolaou, K. Solna, and C. Tsogka. Resolution analysis of passive synthetic aperture imaging of fast moving objects. *SIAM J. Imaging Sciences*, 28, 2017.

[2] Liliana Borcea, Thomas Callaghan, and George Papanicolaou. Motion estimation and imaging of complex scenes with synthetic aperture radar. *Inverse Problems*, 29(5):054011, 2013.

[3] Liliana Borcea and Josselin Garnier. Imaging in random media by two-point coherent interferometry. *SIAM Journal on Imaging Sciences*, 14(4):1635–1668, 2021.

[4] M. Cetin, I. Stojanovic, O. Onhon, K. Varshney, S. Samadi, W. C. Karl, and A. S. Willsky. Sparsity-driven synthetic aperture radar imaging: Reconstruction, autofocusing, moving targets, and compressed sensing. *IEEE Signal Processing Magazine*, 31(4):27–40, July 2014.

[5] M. Cheney and B. Borden. Imaging moving targets from scattered waves. *Inverse Problems*, 24:1–22, 2008.

[6] Margaret Cheney and Brett Borden. *Fundamentals of Radar Imaging*. Society for Industrial and Applied Mathematics, 2009.

[7] J. R. Fienup. Detecting Moving Targets in SAR Imagery by Focusing. *IEEE Transactions on Aerospace and Electronic Systems*, 37(3):794–809, 2001.

[8] Jacques Fournier, Josselin Garnier, George Papanicolaou, and Chrysoula Tsogka. Matched-filter and correlation-based imaging for fast moving objects using a sparse network of receivers. *SIAM Journal on Imaging Sciences*, 10(4):2165–2216, 2017.

[9] Matan Leibovich, George Papanicolaou, and Chrysoula Tsogka. Low rank plus sparse decomposition of synthetic aperture radar data for target imaging. *IEEE Transactions on Computational Imaging*, 6:491–502, 2019.

[10] Matan Leibovich, George Papanicolaou, and Chrysoula Tsogka. Generalized correlation-based imaging for satellites. *SIAM Journal on Imaging Sciences*, 13(3):1331–1366, 2020.

[11] Wei Pu. Deep sar imaging and motion compensation. *IEEE Transactions on Image Processing*, 30:2232–2247, 2021.

[12] Wei Pu. Sae-net: A deep neural network for sar autofocus. *IEEE Transactions on Geoscience and Remote Sensing*, 2022.

[13] L. Wang, M. Cheney, and B. Borden. Multistatic radar imaging of moving targets. *IEEE Trans. Aerosp. Electron. Syst.*, 48(1):230–242, 2012.

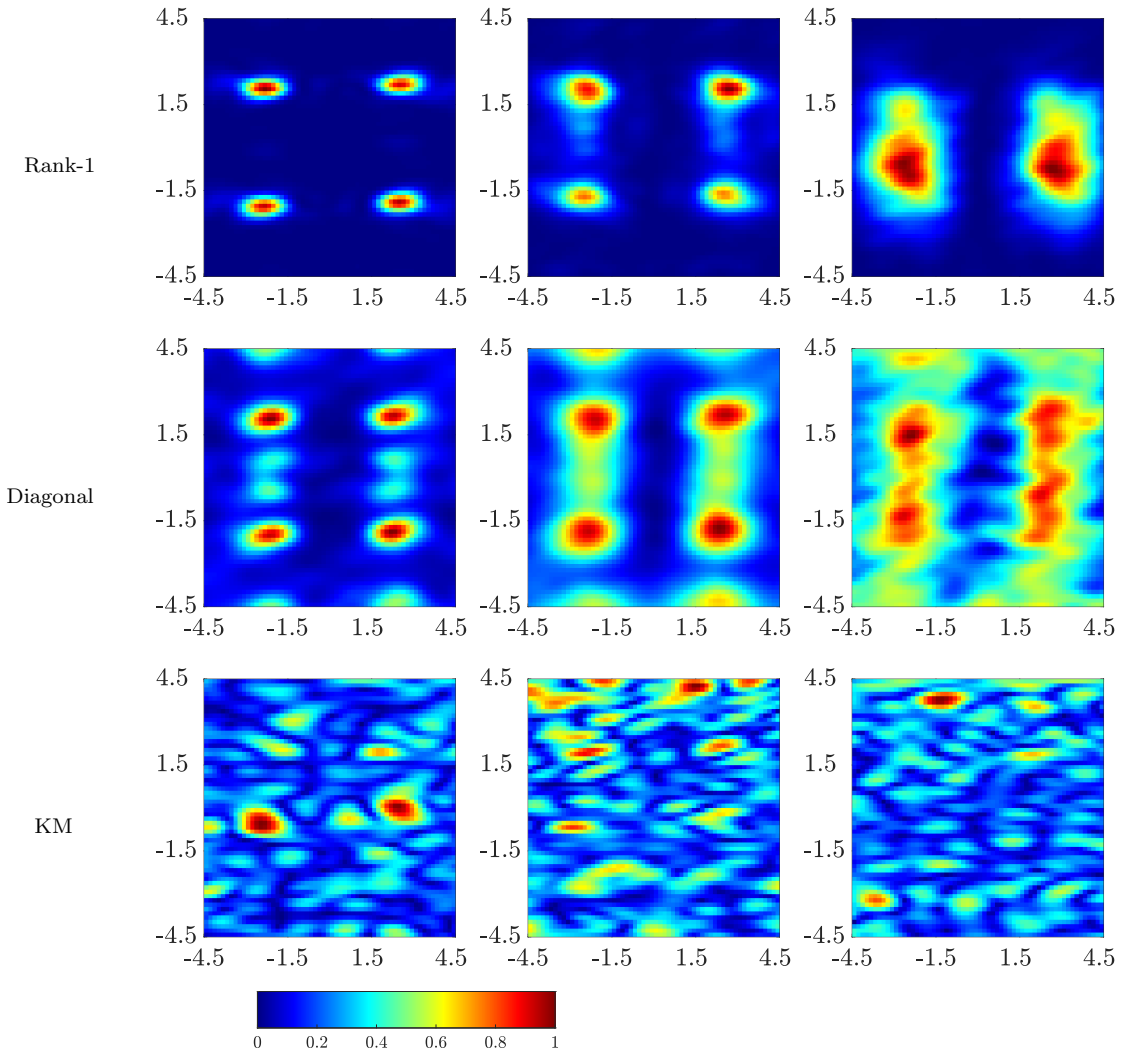

Figure 5: We consider here the case of four scatterers and show results obtained with the three imaging methods as the rms of fluctuations increases. All images are normalized to take values between 0 and 1. From top to bottom: rank-1, diagonal (single point) migration and KM images. From left to right $\sigma = 0.25, 0.55, 1.2$. We observe that the rank-1 image remains stable for higher values of σ compared to the two other methods.

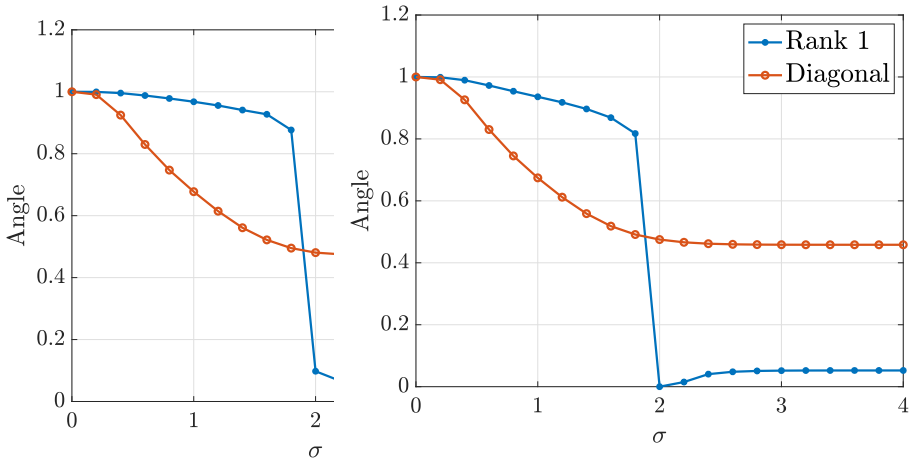

(*a*) 1D simulation.

(*b*) 1D simulation with mean phase approximation

Figure 6: (*a*) Angle between perturbed image and original image as a function of σ for the 1D simulation. (*b*) Same as (a) but where the complex phase is substituted for its mean (see (23)).

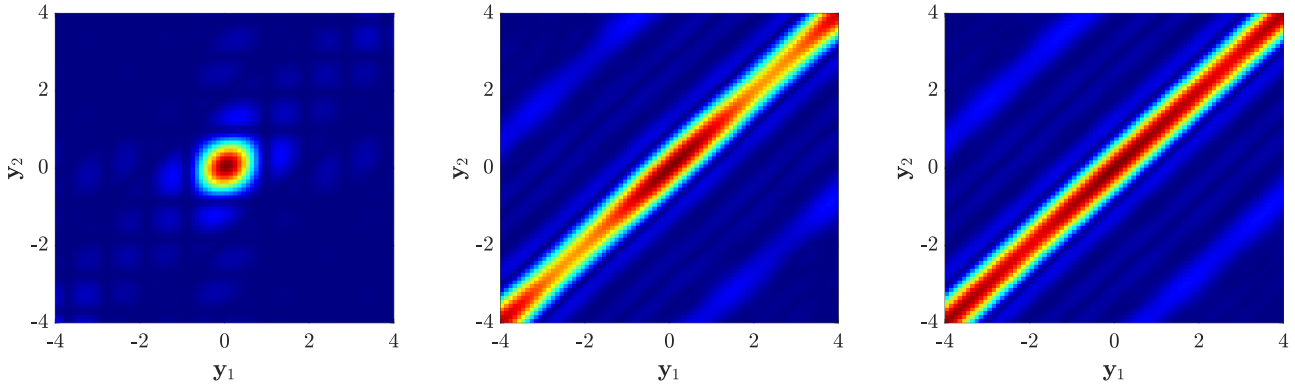

(a) Two point interference function 1D simulation

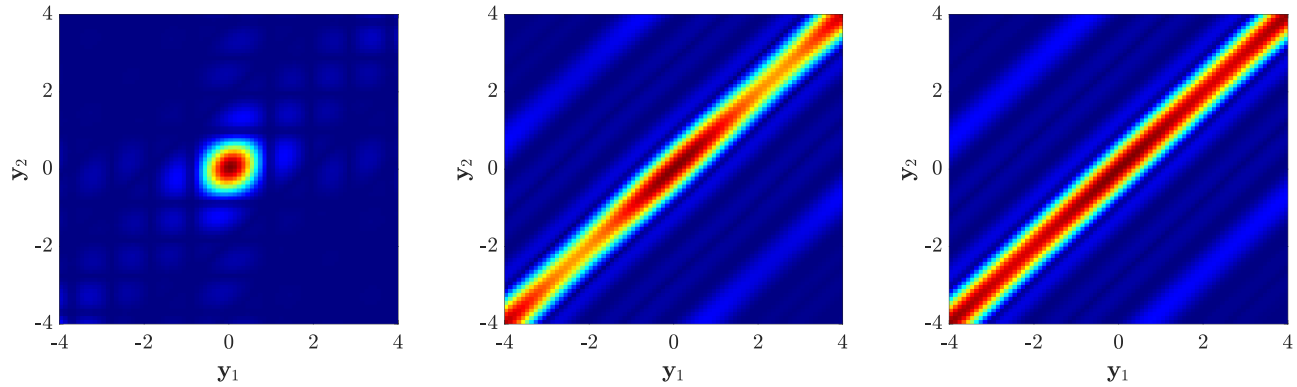

(b)Two point interference function 1D simulation with mean phase approximation

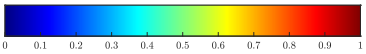

Figure 7: (a) $I(\mathbf{y}_k, \mathbf{y}_{k'})$ for $\sigma = 0, 1.6, 2$ for 1D simulation; (b) $I(\mathbf{y}_k, \mathbf{y}_{k'})$ for $\sigma = 0, 1.6, 2$ for 1D simulation when complex phase is substituted for its mean. All images are normalized to take values between 0 and 1. We can see that the approximation by the mean is well justified by the simulations. Increased fluctuation levels increase the anisotropy, degrading the resolution in the $\mathbf{y}_k - \mathbf{y}'_k$ direction, finally to a point where the target is not localized in the image domain and the rank-1 image breaks down.

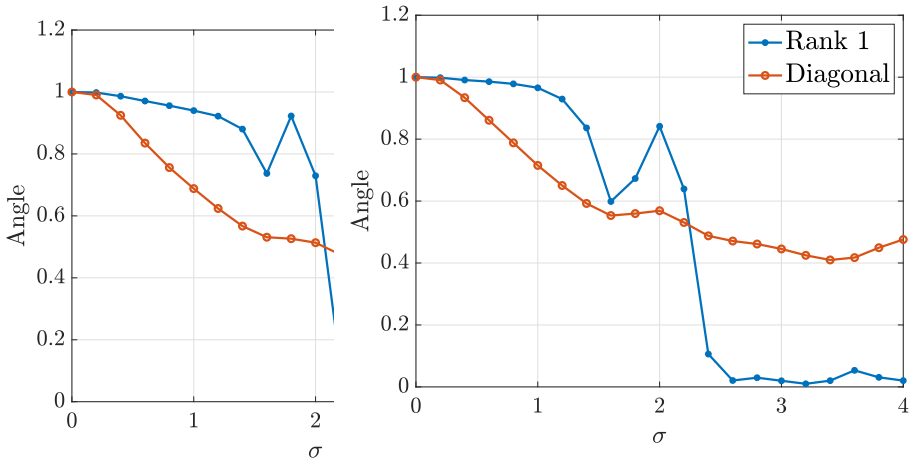

(a) correlation length 200 samples

(b) correlation length 500 samples

Figure 8: Angle as a function of σ for 1D simulation. Noise is now correlated with correlation length of 200 samples (a) and 500 samples (b). The results still exhibit the same behavior